Electro-oxidation of phenol over electrodeposited MnOx nanostructures and the role of a TiO2 nanotubes interlayer

Applied Catalysis B: Environmental 203 (2017) 270–281

Contents lists available at ScienceDirect

Applied Catalysis B: Environmental

journal homepage: www.elsevier.com/locate/apcatb

Electro-oxidation of phenol over electrodeposited MnO_x nanostructures and the role of a TiO_2 nanotubes interlayer

Andrea Massa, Simelys Hernández*, Andrea Lamberti, Camilla Galletti, Nunzio Russo, Debora Fino

Department of Applied Science and Technology (DISAT), Politecnico di Torino, Corso Duca degli Abruzzi 24, 10129 Torino, Italy

ARTICLE INFO

Article history:
Received 27 May 2016
Received in revised form
15 September 2016
Accepted 8 October 2016
Available online 11 October 2016

Keywords:
Manganese oxides
Electrodeposition
TiO_2 nanotubes
Phenol degradation
Electro-oxidation

ABSTRACT

More and more attention has recently been paid to the electrochemical treatment of wastewater for the degradation of refractory organics, such as phenol and its derivatives. The electrodeposition of different types of manganese oxides (MnO_x) over two substrates, namely metallic titanium and titania nanotubes (TiO_2-NTs), is reported herein. X-Ray Diffraction (XRD) and X-Ray Photoelectron Spectroscopy (XPS) analyses have confirmed the formation of different oxidation states of the manganese, while Field Emission Scanning Electronic Microscopy (FESEM) analysis has helped to point out the evolutions in the morphology of the samples, which depends on the electrodeposition parameters and calcination conditions. Moreover, cross section FESEM images have demonstrated the penetration of manganese oxides inside the NTs for anodically deposited samples. The electrochemical properties of the electrodes have been investigated by means of cyclic voltammetry (CV) and linear sweep voltammetry (LSV), both of which have shown that both calcination and electrodeposition over TiO_2-NTs lead to more stable electrodes that exhibited a marked increase in the current density. The activity of the proposed nanostructured samples toward phenol degradation has been investigated. The cathodically electrodeposited manganese oxides (α-MnO_2) have been found to be the most active phase, with a phenol conversion of 26.8%. The anodically electrodeposited manganese oxides (α-Mn_2O_3), instead, have shown higher stability, with a final working potential of 2.9 V vs. RHE. The TiO_2-NTs interlayer has contributed, in all cases, to a decrease of about 1–1.5 V in the final (reached) potential, after a reaction time of 5 h. Electrochemical impedance spectroscopy (EIS) and accelerated life time tests have confirmed the beneficial effect of TiO_2-NTs, which contributes by improving both the charge transfer properties (kinetics of reaction) and the adhesion of MnO_x films.

1. Introduction

The biological treatment of wastewater is one of the most common processes throughout the world for the abatement of a large variety of compounds. However, some organic pollutants, such as aromatic compounds, are refractory and toxic to traditional biological methods. Benzene, phenol and its derivatives (chloro-phenols and nitro-phenols), anilines, benzoquinone and hydroquinone are some of the most common pollutants contained in industrial wastewater [1,2].

Phenol, in particular, is one of the most studied molecules in the sector of the removal of recalcitrant organic compounds from water, due to its high refractoriness and stability, and to its extensive presence in several industrial plants, such as petroleum refineries, and plastics, pesticides and pharmaceutical factories. Advanced oxidation processes (AOPs), such as Fenton and photo-Fenton reactions [3], ozonation [4], wet air oxidation (WAO) [5], catalytic wet hydrogen peroxide oxidation (CWHPO) [6] and catalytic wet air oxidation (CWAO) [7] are all effective methods that can be used to treat this substance. However, electrochemical degradation is another attractive procedure that is being considered to remove recalcitrant organics from water, especially in low-volume applications, due to its intrinsic high efficiency [8,9].

According to the above mentioned classification, electro-oxidation is considered to belong to the AOP family, since OH• radicals, some one of the most powerful oxidizing agents, are produced on the surface of the electrocatalytic materials. Many

Abbreviations: MnO_x, manganese oxides; Ti, titanium; TiO_2-NTs, titania nanotubes; CV, cyclic voltammetries; LSV, linear sweep voltammetries; RHE, reversible hydrogen electrode.

* Corresponding author.
E-mail address: simelys.hernandez@polito.it (S. Hernández).

http://dx.doi.org/10.1016/j.apcatb.2016.10.025

catalysts have been developed for this particular application throughout the years: Pt [10,11], IrO_2 [12,13], RuO_2 [14,15], PbO_2 [11,16], SnO_2 [17,18] and Boron Doped Diamond (BDD) [19,20].

However, only a limited amount of literature has reported the use of manganese oxides (MnO_x) as catalysts for the electro-oxidation of refractory organics [21–26]. Furthermore, in many of these works, the role of manganese oxides has not been investigated in depth because the MnO_x coating had either been deposited onto highly active intermediate substrates, such as Sb-SnO_2 [21] or RuO_2 [22,23], or it had been doped with ions (Fe^{2+}), which can influence the performance of the electrode [24]. MnO_x have been employed extensively in electrochemistry as cathodes in alkaline batteries, in lithium-ion batteries [27] and as pseudo-capacitive electrodes into supercapacitors [28,29], or as photo-anodes for the water splitting reaction [30,31]. The main advantages of manganese oxides is their low cost, if compared to Pt, IrO_2, RuO_2 and BDD, and lower toxicity than Sb-SnO_2 and PbO_2.

This work describes the fabrication and characterization of electrochemically-deposited manganese oxides over a titanium support for the electrochemical oxidation of phenol molecules in wastewater. The electrodeposition parameters, such as current density, deposition time and precursors, were tuned in order to investigate their effect on the activity. Moreover, the effect of the temperature treatment on the electrodeposited MnO_x was investigated by means of calcination in air. Additionally, the role of an interlayer between the MnO_x nanostructures and the Ti substrate was considered, in order to evaluate its effectiveness in preventing the passivation of the Ti substrate and possibly increasing the electrode surface area [32–36]. For these reasons, the optimized parameters described above were used for deposition over a TiO_2 nanotubes (TiO_2-NTs) array, grown directly on Ti foil by means of the anodic oxidation method.

TiO_2-NTs obtained from anodization have attracted considerable interest in the last few decades, since their unique properties make them useful as active elements for several applications, ranging from energy production (dye-sensitized solar cells, [37,38] water splitting, [39,40]) and storage (Li-ions batteries, [41,42] supercapacitors [43]) to sensing devices, such as gas sensing, [44] and molecular sensors [45]. The main advantages of TiO_2-NTs concern their quasi one-dimensional arrangement, which leads to a good compromise between the exposed surface area (about 40 m^2/g) and superior electron transport properties, and results in a performance enhancement in all the different fields of application [46]. Moreover, compared to other synthesis approaches, electrochemical anodization is a simple, convenient and "green" technique to fabricate uniform layers of vertically self-oriented nanostructures, which, furthermore, is easy to be scale up for large-scale industrial productions.

2. Experimental

2.1. Ti substrate preparation

Several $1 \times 2\,cm^2$ titanium (Ti) foils (Sigma-Aldrich, 99.7%, 0.25 mm thick) were mechanically polished with 320-grit sandpaper to obtain a mirror finish, and were then ultrasonically washed in 2-propanol. After rinsing with DI water, the foils were degreased in a 40% NaOH solution at 50 °C for 20 min, and were then rinsed again and left to dry in air.

Shortly, before the electrochemical process, the titanium was etched in an HF (Carlo Erba, 40% w/w) aqueous solution 1.2% w/w, at room temperature for 1 min, in order to obtain a fresh metal surface for NTs growth.

Titania nanotubes were synthesized on the pretreated Ti foils, by dipping $1 \times 1\,cm^2$ into a solution of ethylene glycol, NH_4F (0.5% w/w) and DI water (2.5% w/w). The Ti was used as an anode, while Pt foil was used as both a cathode and a reference electrode. A constant voltage of 60 V was applied to the cell for 10 min and, the TiO_2-NTs were calcined at 450 °C for 30 min after a long rinsing in water. Further details on the NTs growth and characterizations can be found elsewhere [47].

2.2. MnO_x electrodeposition

To the best of the authors' knowledge, no literature reports are available on the direct electrodeposition of manganese oxides onto Ti. In this work, a base-case electrode was anodically deposited by inmersing $1 \times 1\,cm^2$ of the Ti foil or the TiO_2-NTs onto Ti, in an unstirred and undivided cell containing 15 ml of a 0.1 M $Mn(CH_3COO)_2$ and 0.1 M Na_2SO_4 aqueous solution, by applying a current density of 0.25 mA/cm^2 for 10 min (*i.e.* sample *0.25_MnO$_x$*).

The electrodeposition parameters, such as current density, time and Mn-precursor concentration were then varied to investigate their effects on the performances, as shown in Table 1. The samples were named: *ic*_MnO_x/Ti and *ic*_MnO_x/TiO_2-NTs, where *i* is the electrodeposition current density and *c* indicates the calcined samples.

As the current density was found to be the factor with most influence on the morphology and electrochemical behaviour, further syntheses were conducted at 2.5 mA/cm^2, with a deposition time of 10 min and an $Mn(CH_3COO)_2$ concentration of 0.1 M (*i.e.* sample *2.5_MnO$_x$*).

In order to investigate the effects of different electrodeposition techniques, the type of precursor was also changed, once the most suitable current density and deposition time had been tuned. Therefore, cathodic depositions of the manganese oxide over Ti and TiO_2-NTs were then carried out by dipping $1 \times 1\,cm^2$ of Ti foil into an unstirred and undivided cell containing 15 ml of a 0.01 M $KMnO_4$ and 0.1 M Na_2SO_4 aqueous solution, applying a current density of $-2.5\,mA/cm^2$ (*i.e.* sample *-2.5_MnO$_x$*). Fig. 1 presents a schematic view of all the syntheses carried out in this work. Some of the electrodes were calcined at 500 °C for 1 h in air to obtain different manganese oxidation states, and the temperature ramp was also varied to investigate its effect on the possible passivation of the Ti substrate: 2 °C/min (slow) and 20 °C/min (fast).

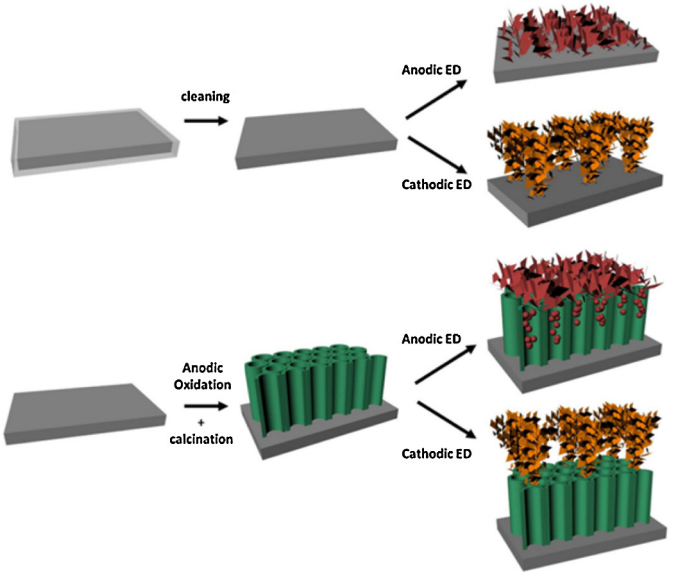

Fig. 1. 3D scheme representing the manganese oxide electrodeposition processes over the Ti and TiO_2 NTs substrates.

Table 1
Manganese oxides electrodes, synthesized by means of electrodeposition over Ti and TiO_2-NTs.

Sample name	ED current (mA/cm^2)	ED time (min)	C_{Mn} (M)	T_{calc} (°C)	Ramp (°C/min)	Precursor	Substrate
0.25_MnO$_x$/Ti	0.25	5–10	0.01–0.1 M	–	–	$Mn(CH_3COO)_2$	Ti
0.25_MnO$_x$/TiO$_2$-NTs	0.25	10	0.1 M	–	–	$Mn(CH_3COO)_2$	TiO_2-NTs
0.25c_MnO$_x$/Ti(s)	0.25	10	0.1 M	500 °C	2	$Mn(CH_3COO)_2$	Ti
0.25c_MnO$_x$/Ti	0.25	5–10	0.01–0.1 M	500 °C	20	$Mn(CH_3COO)_2$	Ti
0.25c_MnO$_x$/TiO$_2$-NTs	0.25	10	0.1 M	500 °C	20	$Mn(CH_3COO)_2$	TiO_2-NTs
2.5_MnO$_x$/Ti	2.5	10	0.1 M	–	–	$Mn(CH_3COO)_2$	Ti
2.5_MnO$_x$/TiO$_2$-NTs	2.5	10	0.1 M	–	–	$Mn(CH_3COO)_2$	TiO_2-NTs
2.5c_MnO$_x$/Ti	2.5	10	0.1 M	500 °C	20	$Mn(CH_3COO)_2$	Ti
2.5c_MnO$_x$/TiO$_2$-NTs	2.5	10	0.1 M	500 °C	20	$Mn(CH_3COO)_2$	TiO_2-NTs
-2.5c_MnO$_x$/Ti	−2.5	10	0.01 M	500 °C	20	$KMnO_4$	Ti
-2.5c_MnO$_x$/TiO$_2$-NTs	−2.5	10	0.01 M	500 °C	20	$KMnO_4$	TiO_2-NTs

A BIOLOGIC VMP-300 potentiostat was used for the electrodepositions. Ti was set as the anode, Pt wire was used as the cathode and Ag/AgCl 3 M KCl (+ 0.209 V vs NHE) was used as the reference electrode.

All the potentials reported in this work should be intended vs. RHE (E_{RHE} in V vs. RHE), and calculated according to Nernst's equation (Eq.(1)):

$$E_{RHE} = E_{Ag/AgCl} + 0.209V + 0.059 \cdot pH \quad (1)$$

2.3. Characterization

The morphology, structure and physic-chemical parameters of the electrodes were evaluated by means of X-Ray Diffraction (XRD, X'Pert PRO diffractomer, Cu Kα radiation λ = 1.54 Å), X-Ray Photoelectron Spectroscopy (XPS, PHI5000 VersaProbe) and Field Emission Scanning Electronic Microscopy (FESEM, Zeiss Merlin). The semi-quantitative surface composition was estimated by means of Electron Energy-Dispersive X-ray spectroscopy (EDX, Oxford X-Act).

2.4. Electrochemical characterization

Cyclic Voltammetries (CV) and Linear Sweep Voltammetries (LSV) were carried out in an unstirred and undivided 3-electrode cell system, containing 15 ml of a 0.1 M Na_2SO_4 solution. The scan limits were fixed between 0.5 and 2 V (vs. Ag/AgCl) and the scan rates were 20 mV/s for the CV and 5 mV/s for the LSV, respectively. The electrode active area was 1 × 1 cm^2; a Pt wire was employed as the counter electrode and an Ag/AgCl 3 M KCl (+ 0.209 V vs. NHE) was used as the reference electrode.

2.5. Electro-oxidation tests

Electro-oxidation tests were carried out in an unstirred and undivided glass cell containing 15 ml of phenol (C_0 = 100 mg/l) and 0.1 M Na_2SO_4 as the supporting electrolyte. The prepared samples (active area of 1 × 1 cm^2) were used as the anode, while Pt wire was set as the cathode and Ag/AgCl, 3 M KCl (+ 0.209 V vs NHE) as the reference electrode. Constant currents were chosen in order to keep the working potential of the electrode under the limit of the instrument (10 V) over a reaction time of 5 h, *i.e.* 0.25 mA/cm^2 for electrodes synthesized at low current densities and 0.75 mA/cm^2 for samples deposited at higher current densities. The solution was then analyzed by High Performance Liquid Chromatography (Shimadzu Prominence HPLC) with a Diode Array Detector (DAD) set at 269 nm. The column was a Rezex ROA (300 × 7.8 mm). The mobile phase was 5 mM H_2SO_4 and the flow rate was 0.5 ml/min. Chemical Oxygen Demand (COD) analyses were carried out by means of UV spectroscopy, using a HACH LANGE COD cuvette test (LCI 400) and a HACH LANGE DR5000 spectrophotometer.

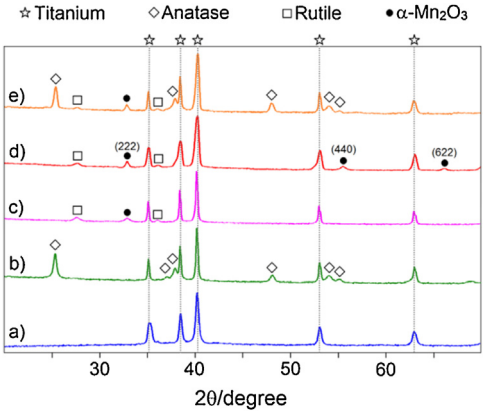

Fig. 2. XRD patterns of MnO_x electrodeposited at 0.25 mA/cm^2, 10 min, 0.1 M Mn^{2+}: a) 0.25_MnO_x/Ti; b) 0.25_MnO_x/TiO_2-NTs; c) 0.25c_MnO_x/Ti (s); d) 0.25c_MnO_x/Ti; e) 0.25c_MnO_x/TiO_2-NTs.

2.6. Accelerated lifetime tests

In order to asses the durability of the synthesized electrodes, accelerated lifetime tests were carried out in an unstirred and undivided glass cell containing 15 ml of a 1 M Na_2SO_4 aqueous solution. Pt wire was used as the cathode and Ag/AgCl, 3 M KCl (+ 0.209 V vs NHE) as the reference electrode. A current density of 100 mA/cm^2 was applied to the cell. The electrode was considered deactivated when the measured potential reached 10 V.

3. Results and discussion

3.1. XRD analysis

Fig. 2 shows the XRD pattern of the manganese oxides electrodeposited at 0.25 mA/cm^2 for 10 min with a 0.1 M of an Mn^{2+} ion concentration, in order to obtain a thicker film and to allow easy detection of the MnO_x peaks.

As expected, non-calcined *0.25_MnO$_x$/Ti* showed no peaks that could be attributed to any crystalline phase of MnO_x (Fig. 2a), thus demonstrating that electrodeposition alone resulted in a non-crystalline material; only Ti peaks were visible [40,48–50].

The *0.25_MnO$_x$/TiO$_2$-NTs* sample (Fig. 2b) showed similar results: the non-calcined manganese oxides did not show any crystalline phase, while TiO_2 peaks were clearly visible and attributable to a tetragonal anatase phase (JCPDS 21-1272, I41/amd, a = b = 0.379 nm, c = 0.951 nm), as expected, due to the calcination of TiO_2-NTs at 450 °C.

Instead, the MnO_x electrodes calcined at 500 °C in air for 1 h, for both the slow (Fig. 2c) and fast ramps (Fig. 2d), showed the particular peaks of a cubic bixbyite crystalline phase, α-Mn_2O_3 (JCPDS

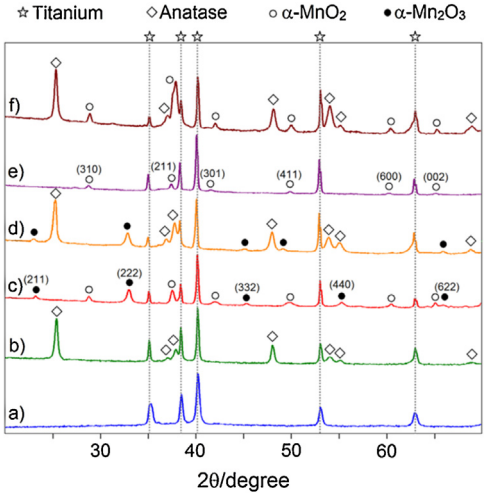

Fig. 3. XRD patterns of MnO_x electrodeposited at 2.5 mA/cm^2, 10 min, 0.1 M Mn^{2+} (or 0.01 M Mn^{7+}): a) 2.5_MnO_x/Ti; b) 2.5_MnO_x/TiO_2-NTs; c) 2.5c_MnO_x/Ti; d) 2.5c_MnO_x/TiO_2-NTs; e) −2.5c_MnO_x/Ti; f) −2.5c_MnO_x/TiO_2-NTs.

41-1442, Ia–3, a = 0.941 nm). The same oxide was obtained over TiO_2-NTs (Fig. 2e).

Moreover, it can be noticed that two peaks appeared, at 27.6° and 36.2°, on the MnO_x calcined samples, on both Ti and TiO_2-NTs. These peaks corresponded to the formation of a TiO_2 rutile phase, whose transition from anatase can start to occur at about 500 °C in air [51–55]. This observation confirmed the hypothesis of the formation of a titanium oxide layer between the Ti substrate and MnO_x coating during the heat treatment.

The XRD patterns of the manganese oxides electrodeposited at 2.5 mA/cm^2 and −2.5 mA/cm^2 are reported in Fig. 3. Such anodically deposited samples, as prepared (*i.e. 2.5_MnO_x/Ti* and *2.5_MnO_x/TiO_2-NTs)*, showed only Ti (Fig. 3a) and TiO_2 anatase (Fig. 3b) XRD patterns, respectively, thus confirming once again that the implemented anodic electrodeposition led to a non-crystalline MnO_x material. Instead, after annealing, the XRD pattern of the *2.5c_MnO_x/Ti* sample (Fig. 3c) showed a noticeable difference, compared to the electrode deposited at 0.25 mA/cm^2. In this case, particular peaks of two MnO_x crystalline phases were detected in the spectrum: a cubic bixbyite α-Mn_2O_3 phase and a tetragonal manganese dioxide α-MnO_2 phase (JCPDS 41-1442, Ia–3, a = 0.941 nm; JCPDS 044-014, I4/m, a = b = 9.7847, c = 2.8630). This result is in contrast with the ones obtained for the same sample obtained at 0.25 mA/cm^2, and it could be possibly due to the different potentials reached during electrodeposition, because of the higher currents provided to the electrode. In fact, a change in either the potential or pH at a constant temperature can have an important effect on the equilibrium of the deposition, and can thus modify the structure of the deposited oxide [56].

In the *2.5c_MnO_x/TiO_2-NTs* sample (Fig. 3d), an intense peak was observed at 32.9°, thus confirming the presence of a α-Mn_2O_3 bixbyite phase in the catalyst film, while α-MnO_2 phase peaks were absent.

The XRD pattern of the tetragonal α-MnO_2 (JCPDS 044-014, I4/m, a = b = 9.7847, c = 2.8630) can be observed for the cathodically deposited electrodes (Fig 3e and f), while no other peaks, apart from those of the substrates, were detected.

In general, the MnO_x electrodes prepared at higher electrodeposition current densities did not show any formation of TiO_2 rutile, as in the case of the ones prepared at lower current density values. This could be due to the higher amount of MnO_x, which covered and protected the Ti substrate and TiO_2-NTs surface from further oxidation.

In order to investigate the surface composition of the electrodeposited MnO_x and to support the XRD analysis outcomes, XPS analysis was carried out on some of the prepared samples: *i.e. 2.5_MnO_x/Ti*, *2.5c_MnO_x/Ti* and *-2.5c_MnO_x/Ti*. The results of the Mn 3 s XPS spectra, with the estimation of the Average Oxidation State (AOS) [57] of the surface of the films are reported in the Supplementary information (SI, Fig. S1 in Supplementary material). It is easy to see that the cathodic sample showed the highest AOS value (*i.e.* 3.56), which was close to the Mn^{4+}, identified by the XRD. Instead, the AOS value for the *2.5c_MnO_x/Ti* was 3.11, which is also in agreement with the presence of a mix of Mn oxides with oxidation states of Mn^{3+} and Mn^{4+}, as revealed by the XRD measurement. Finally, the non-calcined MnO_x, whose oxidation state could not be identified by means of XRD, gave an intermediate AOS value (*i.e.* 3.25), which probably means that also a mixed oxide Mn^{3+}/Mn^{4+} could have been formed after the electrodeposition, but with a slightly higher presence of Mn^{4+} than the anodically deposited calcined sample.

3.2. FESEM and EDX analyses

Fig. 4 reports the FESEM images of the manganese oxides electrodeposited at 0.25 mA/cm^2. The FESEM cross-section images of the TiO_2 nanotubes, after the anodization process, are shown in Fig. 4a. The NTs were 5 μm long and vertically aligned with respect to the Ti foil. The ordered distribution of the pores can be appreciated in the top FESEM image reported as an inset in Fig. 4a: the inner holes had an average dimension of about 70 nm and a wall thickness of around 20 nm. After the MnO_x electrodeposition, the typical formations of nanoflake structures, which have also been observed in other works [40,50,58], were formed for all the different types of electrodes. The thickness of the manganese oxide layer (∼623 nm) was quite uniform, as can be seen in the inset in Fig. 4b. A slight change in the morphology can be noticed when *0.25_MnO_x/Ti* (Fig. 4b) is compared with *0.25c_MnO_x/Ti,* which was calcined with the fast ramp at 20 °C/min (Fig. 4e), however still maintaining the overall nanoflake disposition. The electrode calcined with a slow ramp, that is, *0.25c_MnO_x/Ti(s)* (Fig. 4d), instead, presented an almost unchanged nanoflakes structure with respect to *0.25_MnO_x/Ti*. Both samples grown on NTs, that is, the not calcined *0.25_MnO_x/TiO_2-NTs* (Fig. 4c), and the calcined *0.25c_MnO_x/TiO_2-NTs* samples (Fig. 4f), showed nanoflake on the top of the nanotube layer. The deposition of nanoflakes on the TiO_2-NTs substrate was less homogeneous than the deposition on metallic titanium, showing some uncovered areas, probably due to preferential pathways of the electrodeposition currents, where the electric resistance was lower.

Fig. 5 shows the FESEM images of the manganese oxide electrodeposited at 2.5 mA/cm^2 and −2.5 mA/cm^2. The non calcined anodically deposited samples, *i.e. 2.5_MnO_x/Ti* (Fig. 5a) and *2.5_MnO_x/TiO_2-NTs* (Fig. 5b), still showed a similar nanoflake structure to the one seen for the sample synthesized at lower current densities. However, the nanoflakes were smaller for both electrodes, due to the higher electrodeposition current density. In fact, the nucleation rate is higher and the critical nucleation radius is decreased, as the potential and current density are increased, thus the formation and refinement of the initial grain are improved [56]. The inset in Fig. 5a allows the thickness of the MnO_x film on the *2.5_MnO_x/Ti* sample (∼3.7 μm), which was six times higher than the one on the samples obtained with 0.25 mA/cm^2, to be appreciated. The calcined *2.5c_MnO_x/Ti* (Fig. 5c) and *2.5c_MnO_x/TiO_2-NTs* samples (Fig. 5d), instead, showed very fine nanoflakes, that coexisted with another type of larger crystalline nanoparticles, which were present in a greater amount on the sample grown on the titanium substrate. Such a difference in morphology can be explained by considering the larger amount of the α-MnO_2 phase in the elec-

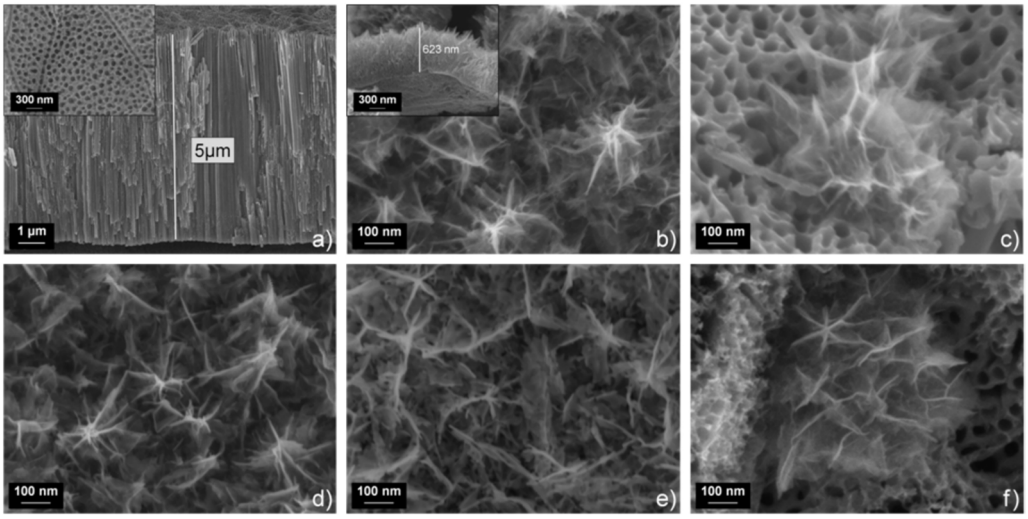

Fig. 4. FESEM images of the samples electrodeposited at 0.25 mA/cm^2: a) TiO_2-NTs; b) 0.25_MnO_x/Ti; c) 0.25_MnO_x/TiO_2-NTs; d) 0.25c_MnO_x/Ti (s); e) 0.25c_MnO_x/Ti; f) 0.25c_MnO_x/TiO_2-NTs.

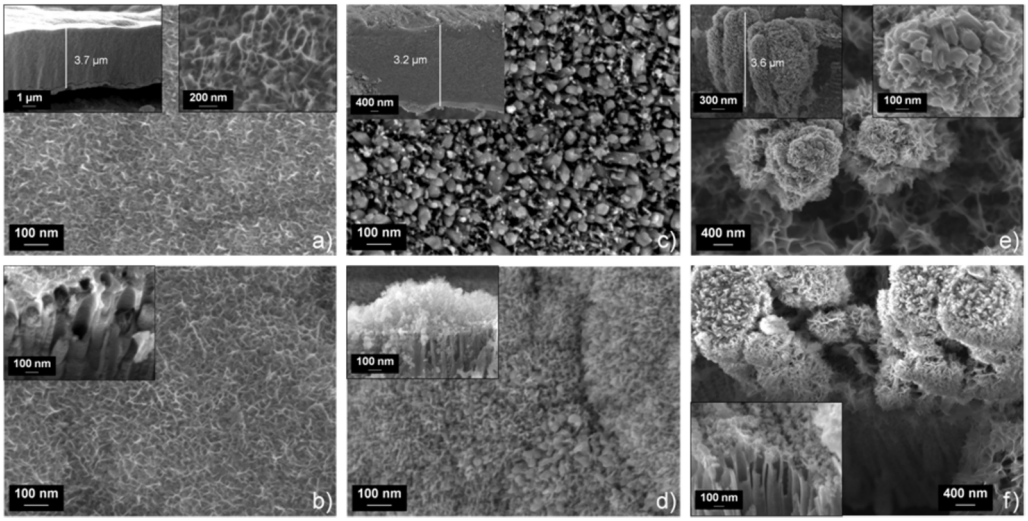

Fig. 5. FESEM images of the samples electrodeposited at 2.5 mA/cm^2: a) 2.5_MnO_x/Ti; b) 2.5_MnO_x/TiO_2-NTs; c) 2.5c_MnO_x/Ti; d) 2.5c_MnO_x/TiO_2-NTs; e) −2.5c_MnO_x/Ti; f) −2.5c_MnO_x/TiO_2-NT.

trode grown on Ti, as observed in the XRD analysis, which more likely composes the larger nanoparticles.

Unlike the samples electrodeposited at 0.25 mA/cm^2, the cross-sectional view of the *2.5_MnO_x/TiO_2-NTs* and *2.5c_MnO_x/TiO_2-NTs* samples exhibited evidence of the penetration of the manganese inside the nanotubes structure, as shown in the inset of Fig. 5b and d, similarly to the penetration of the electrodeposited Sb-doped SnO_2 films into TiO_2-NTs [32]. This phenomenon was probably due to the high electrodeposition current densities which led to smaller nanoflakes that were able to grow inside the nanotube.

The FESEM images of the MnO_x samples, that is, *-2.5c_MnO_x/Ti* (Fig. 5e) and *−2.5c_MnO_x/TiO_2-NTs* (Fig. 5f), prepared by cathodic deposition, pointed out a totally different morphology from the anodically deposited MnO_x. The nanoflakes formed a layer directly over the nanotubes, from which polycrystalline rod-like structures of a noticeable thickness (~3.6 μm) grew. In this case, the cross-section of the *−2.5c_MnO_x/TiO_2-NTs* sample, shown as an inset in Fig. 5f, did not report a deep penetration of manganese oxide inside the nanotubes. This could be due to either a different wettability of the nanotubes by the $KMnO_4$ solution from the $Mn(CH_3COO)_2$ used in the anodic deposition, or a different electric field induced inside and on the top of the nanotubes.

Tables 2 and 3 show some of the data from the EDX surface composition analyses of all the manganese oxides over Ti and TiO_2-NTs. As can be noticed, for all the samples synthesized at 0.25 mA/cm^2, the atomic ratio (Mn/Ti) is comparable, with a slightly higher manganese content for the non-calcined electrode grown on nanotubes (*i.e. 0.25_MnO_x/TiO_2-NTs*). For samples synthesized at 2.5 or −2.5 mA/cm^2, the atomic ratio, Mn/Ti, is up to 10 or even 100 times higher than the one reported for the electrodes synthesized at lower current densities, as a greater amount of manganese oxide was deposited on these samples. Moreover, the Mn/Ti values measured for the films grown on Ti, were considerably higher than the ones registered for those grown on the nanotubes, and this could be due to the higher electric resistance of the TiO_2-NTs than the metallic Ti, which limited the total amount of manganese oxide deposited. However, because of the higher surface area of the TiO_2-NTs, it is more likely that the lower Mn/Ti ratios observed in the NTs than on Ti were due to the better distribution of MnO_x on

Table 2
Electrooxidation results for 0.25_MnO_x electrodes. El-Ox current density 0.25 mA/cm^2.

Electrode	MnO_x phase[a]	Mn/Ti ratio[b]	Faradaic efficiency (%)	TON (mol_{Phenol}/mol_{Mn})	Relative conversion ($mol_{Phenol}/mol_{Mn} \cdot W \cdot h$)
0.25_MnO_x/Ti	Non-crystalline	0.12	7.8	0.25	37.2
0.25_MnO_x/TiO_2-NTs	Non-crystalline	0.16	33.2	2.36	469.0
0.25c_MnO_x/Ti	α-Mn_2O_3	0.11	10.7	0.86	212.6
0.25c_MnO_x/TiO_2-NTs	α-Mn_2O_3	0.11	37.1	1.15	314.8
Ti	–	–	0.0	–	–
TiO_2-NTs	–	–	22.4	–	–

[a] From XRD patterns.
[b] Calculated from EDX.

Table 3
Electrooxidation results for 2.5_MnO_x electrodes. El-Ox current density 0.75 mA/cm^2.

Electrode	MnO_x phase[a]	Mn/Ti ratio[b]	Faradaic efficiency (%)	TON (mol_{Phenol}/mol_{Mn})	Relative conversion ($mol_{Phenol}/mol_{Mn} \cdot W \cdot h$)
2.5_MnO_x/Ti	Non-crystalline	15.2	43.3	0.51	17.1
2.5_MnO_x/TiO_2-NTs	Non-crystalline	2.11	42	0.48	20.1
2.5c_MnO_x/Ti	α-Mn_2O_3/ α-MnO_2	18.15	45.9	0.35	25.1
2.5c_MnO_x/TiO_2-NTs	α-Mn_2O_3	1.59	26.7	0.26	25.7
-2.5c_MnO_x/Ti	α-MnO_2	13.4	44.6	0.82	43.7
-2.5c_MnO_x/TiO_2-NTs	α-MnO_2	7.44	45.3	0.75	46.7

[a] From XRD patterns.
[b] Calculated from EDX.

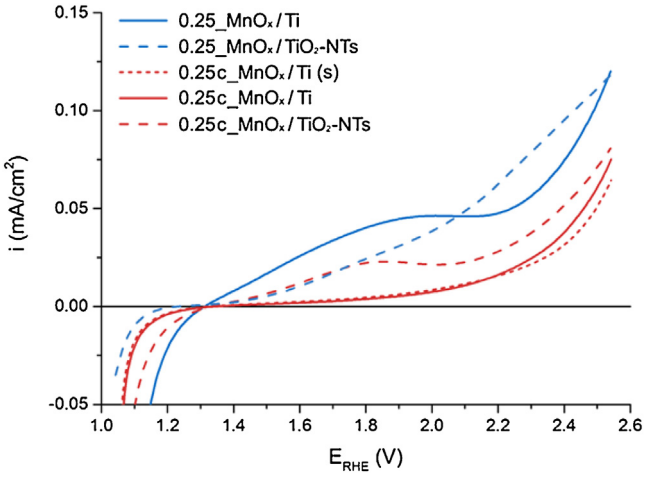

Fig. 6. LSV in 0.1 M Na_2SO_4 of the samples electrodeposited at 0.25 mA/cm^2.

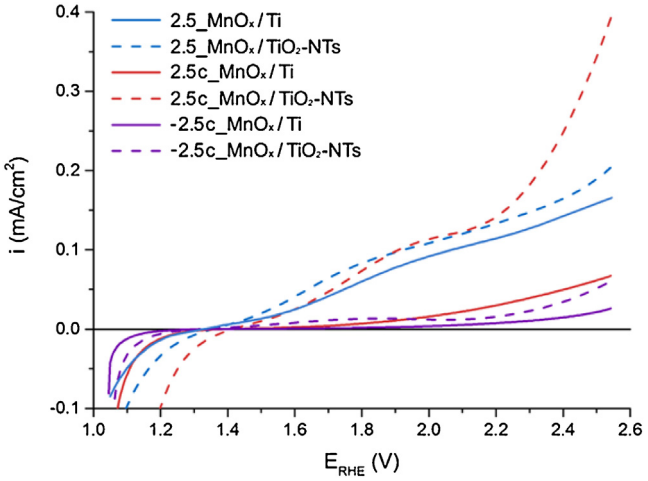

Fig. 7. LSV in 0.1 M Na_2SO_4 of the samples electrodeposited at 2.5 and −2.5 mA/cm^2.

the top of the TiO_2-NTs, as well as inside the NTs pores (Fig. 5b and d).

3.3. Electrochemical behaviour

Figs. 6 and 7 show the LSV of all the manganese oxide samples electrodeposited at 0.25 mA/cm^2 and 2.5 mA/cm^2, respectively, at a scan rate of 5 mV/s. The as-prepared (non-calcined) cathodic samples are not shown because they demonstrated very poor current densities and became detached from the substrate after just few cycles. In both graphs, the non-calcined *MnO_x/Ti* (Figs. 6a, 7a) and all the samples anodically grown on the NTs (dashed lines in Figs. 6b and e, 7b and d) showed pseudo-capacitive behaviour, which is characteristic of crystalline MnO_2, or non-crystalline MnO_x phases [39] and which could also be due to titania nanotubes [39,41,42]. The pseudo-capacitance in the MnO_x phase was caused by the electron transfer at the Mn surface sites, the charge transfer being balanced by either the chemisorption/desorption of the electrolyte cations or by the insertion/desinsertion of the protons [39,59]. In the case of TiO_2, due to its semiconducting properties, electrons are accumulated in the material when it behave like a cathode (*i.e.* presence of negative current values), and are then released when the electrode polarity is inverted and acts as an anode [39]. The CVs of the non-calcined manganese oxides, for the depositions at both 0.25 mA/cm^2 and 2.5 mA/cm^2 (see SI, Figs. S2–S7 in Supplementary material), also confirmed the high capacitance characteristic, which was more evidently reported for the electrodes grown on the nanotubes. In addition, although the current densities were similar, the manganese oxides grown on nanotubes showed a slight increment in stability after 5 CV cycles.

Instead, the LSVs of the calcined *MnO_x/Ti* samples (Figs. 6c, d and 7c) showed a diminuation of the capacitive properties of the film, due to the change in the crystalline phase, from non-crystalline or α-MnO_2 to α-Mn_2O_3 [40], or because of the variations in the morphology (growth in the particle sizes) of the deposited film after the thermal treatment [60]. On the other hand, the calcined *MnO_x/TiO_2-NTs* sample containing α-Mn_2O_3, still showed a capacitive trend, probably because of the residual capacitance of the nanotubes in the interlayer [39].

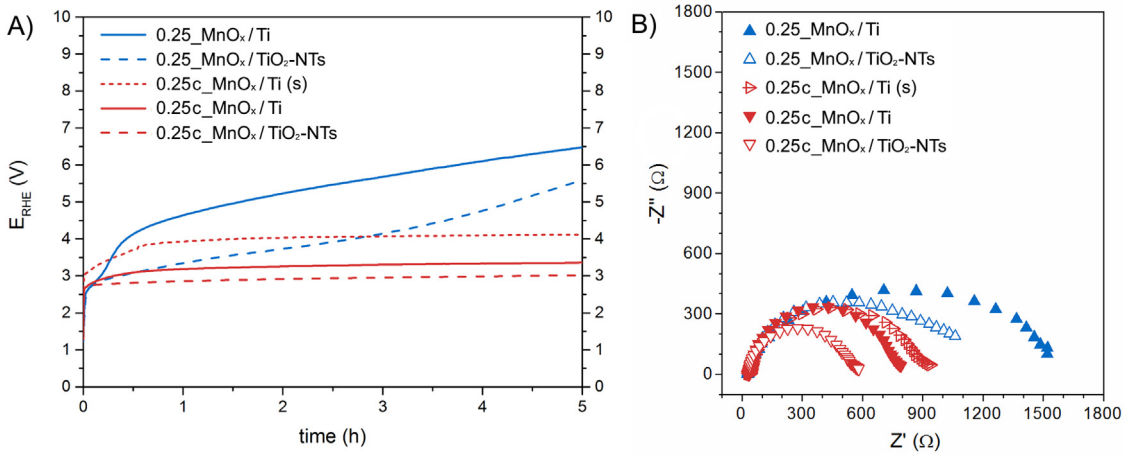

Fig. 8. (A) Electro-oxidation curves at 0.25 mA/cm^2 and (B) Nyquist plots of the EIS measurements at 3.3 V vs. RHE. of samples synthesized at 0.25 mA/cm^2.

As far as the MnO_x cathodically deposited on both Ti and TiO_2-NTs is concerned (Fig. 7e and f), although the prevalent phase formed after their thermal treatment was α-MnO_2, they showed a flat LSV and low current densities (<0.05 mA/cm^2 at 2.5 V vs. RHE) towards the water oxidation reaction. Such phenomena could be explained by considering the different rod-like morphologies of these MnO_x samples, which have less exposed surface area than the nanoflakes, and this could lead to a lower capacitive effect. It has been reported that differences in MnO_2 morphology under different electrodeposition conditions and the post-thermal treatments could contribute to the differences in the capacitive behaviours [61,62]. Indeed, a lower capacitance effect has been observed for a smaller nanosheets spacing and more compactness of the structure, which make ion diffusion within the structure difficult [61]. Moreover, the interaction with the substrate seems to play a crucial role in the capacitive behaviour of manganese oxide films, and also leads to different morphologies, which in turn affects the electrochemical characteristics of the electrode [63,64].

In general, the CVs (see SI, Figs. S2 to S7 in Supplementary material) showed an improved stability for the calcined MnO_x samples, as well as for all the samples deposited on TiO_2-NTs, possibly because the passivating TiO_2 layer that usually formed on the Ti surface under oxidative conditions [33,36], was prevented from forming by the presence of either well crystallized manganese oxides structures (formed after calcination) or crystalline TiO_2-NTs.

The LSVs of the as-prepared and calcined electrodes synthesized at 0.25 mA/cm^2 with different electrodeposition times (10 vs. 5 min) and precursor concentrations (0.1 vs. 0.01 M Mn^{2+}) are reported in the SI (Figs. S8 and S9 in Supplementary materail, respectively). As can be noticed, both the shape of the curves and the current density values were similar, and it is therefore possible to state that these two parameters did not affect the electrochemical behaviour of the samples to any great extent. For this reason, 10 min and 0.1 M Mn^{2+} were selected as the optimum conditions for the electrodepositions at higher current densities (*i.e.* 2.5 mA/cm^2).

The *2.5c_MnOx/TiO2-NTs* sample produced the highest final current density (~0.4 mA/cm^2 at 2.5 V vs. RHE, see Fig. 7d), which was one order of magnitude higher than the similar MnO_x film deposited on Ti (*2.5c_MnOx/Ti*,), and than the cathodically deposited films (*-2.5c_MnOx/Ti* and *−2.5c_MnOx/TiO2-NTs*). Moreover, it was two times higher than the current densities obtained for the respective non calcined samples, on both Ti and TiO_2-NTs. This trend was in agreement with the predominance of the α-Mn_2O_3 phase revealed by the XRD analysis on the calcined electrodes containing TiO_2-NTs, which is capable of higher oxygen evolution rates than α-MnO_2 [23,30,50], thus justifiyng the improved behaviour for the water oxidation reaction. On the contrary, the presence of α-MnO_2 detected on the sample grown on Ti, as well as in the cathodically deposited MnO_x, led to a decrease in the water oxidation activity [65,66], which instead should be beneficial for the degradation of organic molecules (*e.g.* phenol) with a higher Nernst potential than water oxidation.

3.4. Phenol electro-oxidation and EIS analysis

Figs. 8A and 9A show the chrono-potentiometric curves obtained during the phenol electro-oxidation (El-Ox) reaction with all the electrodes synthesized at 0.25 mA/cm^2 and 2.5 or −2.5 mA/cm^2, respectively. Electro-oxidation was performed for a total time of 5 h, fixing a current density of 0.25 mA/cm^2 for the *0.25_MnOx* samples, while the *2.5_MnOx* electrodes were tested at 0.75 mA/cm^2, in order to start the El-Ox at about 3 ± 0.5 V_{RHE} and to keep the final working potential below 10 V. In addition, electrochemical impedance spectroscopy (EIS), a well-known technique that is often employed to characterize electrochemical systems with the aim of comparing their charge transfer and transport properties [37,39,67], was also performed on the phenol solution. An applied DC potential of 3.3 V_{RHE}, which was the average initial potential achieved during the El-Ox process for all the samples, was employed for the EIS analyses. The results are reported in Figs. 8B and 9B (Nyquist plots) and in Fig.s S10 and S11 (Bode plots: phase and modulus of impedance |Z| vs. frequency).

The most stable electrodes that were able to sustain the constant potential (*i.e.* for which the total increase of potential over time was lower than 0.5 V) were found to be the calcined anodically deposited MnO_x electrodes over both the Ti and TiO_2-NTs subtrates (see Figs 8A-c,d,e and 9A-c,d), which can be attributed to the presence of highly stable α-Mn_2O_3 crystalline phase. Accordingly, the Nyquist plots of the same samples in Figs. 8B and 9B show that they evidenced lower impedance values for these electrodes than for the other electrodes, which in turn indicated an increase in the number of electrons transferred through the electrode/electrolyte interface on those materials. In fact, a reduction in the semicircles diameter in the Nyquist plots indicated a lower resistance to the charge transfer because of an enhancement of the reaction kinetics, which, in this case, depends on the surface properties of the MnO_x-based electrode materials [40]. Nevertheless it is not possible to identify which is the prevalent reaction between water oxidation and phenol degradation from these electrochemical measurements, and, the phenol and COD conversion were therefore chemically determined and are reported in Section 3.5.

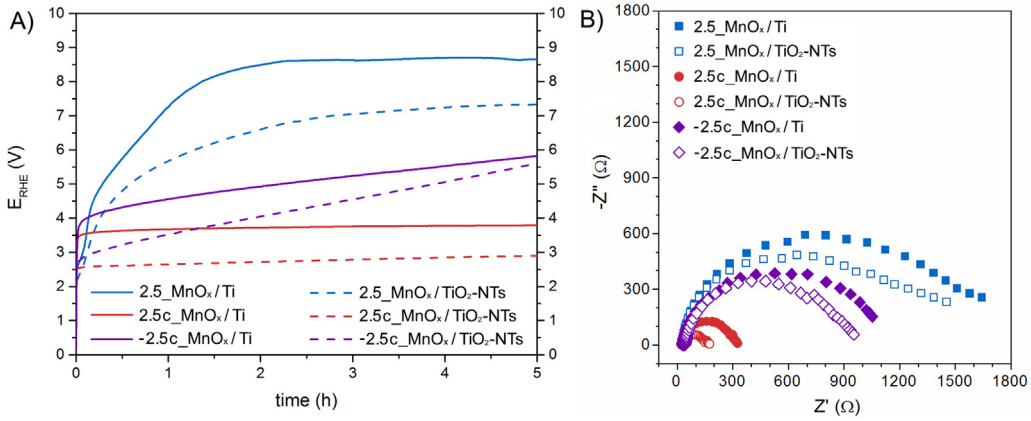

Fig. 9. (A) Electro-oxidation curves at 0.75 mA/cm^2 and (B) Nyquist plots of the EIS measurements at 3.3 V vs. RHE of samples synthesized at 2.5 mA/cm^2.

Instead, all the as-prepared MnO_x samples (Figs. 8a, b, 9a, b) reached very high potentials, of up to 8.6 V. An intermediate behaviour was observed for the thermal-treated cathodically deposited MnO_x samples, which were constituted by rod-like α-MnO_2, and steadily increased the potential up to 6 V.

Interestingly, in all the samples, TiO_2-NTs contributed to reduce the applied potential for phenol El-Ox (from 0.5 to 1.5 V) with respect to the Ti substrate. In particular, the *0.25c_MnO$_x$/Ti* and *2.5c_MnO$_x$/Ti* samples settled at a higher potential (of about 0.4 V and 1 V, respectively) than the similar materials deposited on the TiO_2-NTs substrates. This trend can be attributed to the presence of a certain amount of α-MnO_2 for the *2.5c_MnO$_x$/Ti* sample, but not for the other material.

Besides, the difference between the El-Ox potential of the MnO_x on the Ti, for the non-crystalline MnO_x electrodes (Figs 8A and 9A), with respect to that on the TiO_2-NTs substrate increased during the time-course of the reaction. On the other hand, TiO_2-NTs interlayer in cathodically deposited electrodes (Fig. 9A), did not decrease the potential with respect to the sample on Ti in the same extent as the anodically deposited MnO_x, but a certain improvement was also achieved in this case. A possible explaination for such behaviour could be the lower tendency of the cathodically deposited manganese oxide to enter the nanotube pores, as already observed in the FESEM cross-sections (Fig. 5f), and, to a certain extent, could also be due to a loss of adhesion of the MnO_2 to the substrate.

In short, the positive influence of the NTs subtrate on the behaviour of the electrodes was evident as it increased the reaction kinetics and led to a lowering of the necessary potential, which was also demonstrated by the lower impedance of the MnO_x samples deposited on TiO_2-NTs than their counterparts supported on the Ti foils, as can be seen in Figs 8B and 9B and in the modulus of impedance |Z| at 1 Hz reported in Figs. S10 and S11 in the SI.

Since the charge transport differences in the samples were not so evident in the Nyquist plots in Figs 8B and 9B, the EIS measurements were also plotted in the form of Bode diagrams (Fig.s S10 and S11 in the SI). Bode plots are usually useful to separate charge transfer and charge transport processes in electrochemical systems because the latter is characterized by faster time constants [30,67]. The phase spectra in Fig.s S10 and S11 show a clearly distinguishable peak for all the electrodes in the range between 100 and 1000 Hz (aprox. centered at about 200 Hz for most of the samples), which can be attributed to the charge transport process in such electrodes [39,40]. Instead, the charge transfer process at the electrode/electrolyte interface can be analyzed from the |Z| at frequencies lower than 100 Hz, in the same way as for previous works [39,40]. For comparison purposes, the |Z| values at 200 Hz and at 1 Hz could be ascribed to a measure of the charge transport and charge transfer resistances, respectively, of the different electrodes. As expected, the values of |Z| at 1 Hz followed an equivalent trend to the diameter of the Nyquist plots semicircles, and the same conclusions as before can therefore be drawn.

In the thin samples (see the FESEM images in Fig. 4) deposited at 0.25 mA/cm^2, the highest conductivity of the Ti substrate is confirmed by the low |Z| values (*e.g.* 58 Ω at 200 Hz) of the non-calcined MnO_x sample supported on Ti foil (*i.e. 0.25_MnOx/Ti*). Obviously, such resistance values also accounted for the resistivity of the non-crystalline MnO_x film towards the electrons flow and, consequently, it could not be null. As a consequence, the charge transport resistance was higher for the sample deposited on the TiO_2-NTs, with a |Z| value of 118 Ω at 200 Hz, which can be attributed to the lower conductivity of TiO_2 than the metallic Ti.

However, after the thermal treatment, the charge transport was similar, with a higher value of |Z| for all the samples. The sample calcined with the slow ramp, *0.25c_MnO$_x$/Ti (s)*, showed the highest impedance (*i.e* 257 Ω at 200 Hz), while the fast heating ramp decreased the impedance to 172 and 198 Ω in the *0.25c_MnO$_x$/Ti* and *0.25c_MnO$_x$/TiO$_2$-NTs* samples, respectively. Considering that all these calcined samples contained α-Mn_2O_3, their charge transfer properties can be attributed to the formation of the TiO_2 passivation layer on the surface of the Ti foil (as observed from the XRD), which caused a considerable drop in the metallic behaviour of this substrate, especially for the slow heating ramp, which exposed the sample to high temperatures for longer times.

The electric conduction properties of the TiO_2 nanotube arrays are mainly related to defects produced during the electrochemical growing process (anodization), which lead to the well-known n-type semiconducting behaviour. Oxygen vacancies and Ti^{3+} states in TiO_2 nanotubes, which dominate optical and electrical properties of the material to a great extent [46] are particularly important. In comparison to a compact oxide layers, such as the thermal oxide formed under the MnO_x (on Ti) after annealing, the doping level obtainable inside the crystalline TiO_2 nanotubes is generally very high (10^{20} cm^{-3}, as calculated by Mott–Schottky analysis in a previous work [42]). This can explain the different behaviour observed for the *0.25_MnO$_x$/Ti* and *0.25c_MnO$_x$/Ti* samples in comparison with their counterparts in TiO_2 NTs. The metallic behaviour of titanium in the non-crystallized sample leads to a higher charge transport from the MnO_x to the current collector, while the rutile layer without defects that is formed on the top of the metal substrate after calcination at 500 °C becomes less effective than the self-doped nanotubular carpet, despite their different thicknesses.

On the other hand, when the MnO_x amount and the film thickness is increased, after an increase in the electrodeposition current to 2.5 mA/cm^2, both of the non-calcined samples on Ti foil and

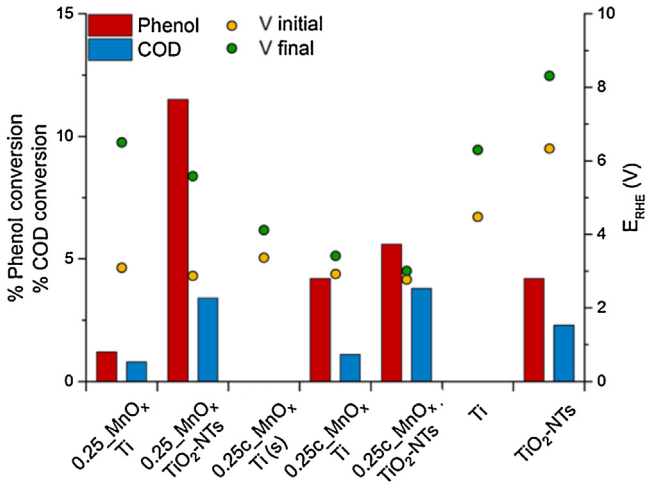

Fig. 10. Phenol and COD reduction, initial and final potentials for the electrooxidation test of the samples synthesized at 0.25 mA/cm^2 and for Ti and TiO_2-NTs substrates.

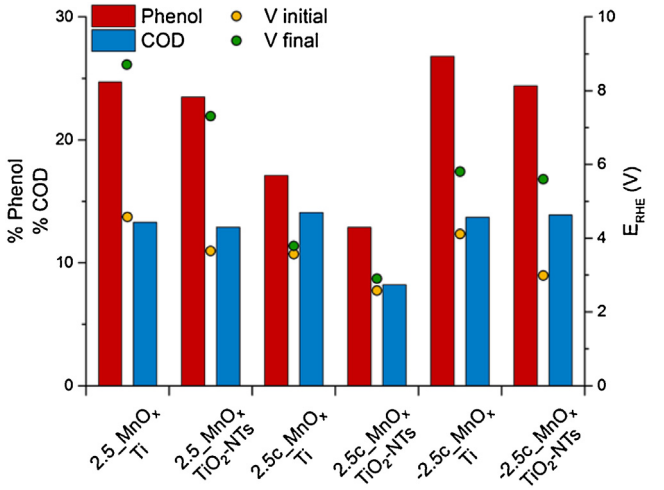

Fig. 11. Phenol and COD reduction, initial and final potentials for electrooxidation test of samples synthesized at 2.5 mA/cm^2.

TiO_2-NTs reported similar |Z| values (*i.e* 100 Ω at 200 Hz). After the thermal treatment, their charge transport resistance increased slightly, showing |Z| values of 133 and 115 Ω, respectively, at 200 Hz, which once again is probably due to the formation of a passivating layer after the calcination. Moreover, the impedance modulus was higher for the *2.5c_MnO$_x$/Ti* sample, which contained α-Mn_2O_3 and α-MnO_2, unlike the sample on the TiO_2-NTs which only contained α-Mn_2O_3, as observed from the XRD analyses.

In the case of the calcined cathodically deposited samples, although both were constituted by α-MnO_2, the one on the Ti substrate reported a lower charge transport resistance than the similar sample on TiO_2-NTs, which had a |Z| value at 200 Hz of about 59 Ω and 200 Ω, respectively. In this case, the poor charge transport could be due to the limited contact area between the α-MnO_2 film and the nanotubes, as shown by the cross section of the FESEM images.

3.5. Phenol and COD conversion

Fig. 10 and Table 2 report the phenol degradation results obtained for the electrodes synthesized at 0.25 mA/cm^2 on both Ti and TiO_2-NTs. The results obtained for the two substrates, without any catalyst, are also reported for comparison purposes. Phenol and COD conversion, together with the potential values, shown in Fig. 10, are listed in Table S1 (SI) in Supplementary material. The effects of the electrodeposition time and concentration of the Mn^{2+} precursor are shown in Fig. S8B for the non-calcined electrodes, and in Fig. S9B for the calcined samples. As can be observed, neither of these parameters influence the efficiency or the stability to any great extent.

Although the conversions were rather low for most of the electrodes, an interesting trend can be observed: the nanotubes interlayer seems to have a beneficial effect on both the degradation and the maximum potential reached after 5 h of reaction. In particular, the non-calcined *0.25_MnO$_x$/TiO$_2$-NTs* sample reported the highest phenol conversion, that is, of about 12%.

It is also worth noticing that the blank test with the TiO_2-NTs substrate showed a slight conversion of phenol (about 4%), unlike the Ti foil, which was totally unactive. The nanotubes resulted in a comparable conversion to that of the calcined electrodes, which indicates a higher selectivity of the non-crystalline MnO_x than of the sample containing α-Mn_2O_3 for this reaction; however, the reduction of the potential (more than 3 V) necessary to perform the reaction in the presence of the manganese oxide catalysts on the TiO_2-NTs, is clear, which confirmed the effectiveness of these materials for phenol degradation. As discussed in Section 3.4, the role of TiO_2-NTs is related to a decrease in the charge transfer resistance (*i.e.* kinetics of reaction), which is probably induced by the good distribution and penetration of the manganese oxide on the high surface area and by the porosity provided by this 3D nanostructure, which enhance the diffusion of the electrolyte to the active material [32,33,62,68].

As far as the effect of the temperature ramp during calcination is concerned, the electrode calcined at the slow ramp of 2 °C/min (*0.25c_MnO$_x$/Ti (s)*) did not lead to any conversion and resulted in a higher final potential than the similar sample calcined with a fast heating ramp (20 °C/min, sample *0.25c_MnO$_x$/Ti*). Therefore, the latter condition was implemented for the subsequent studies. Under such a condition, calcination improved the stability of all the samples and acted positively on the phenol conversion in the case of the sample on the Ti substrate (*0.25c_MnO$_x$/Ti*).

Fig. 11 and Table 3 show the performances obtained for the samples deposited at 2.5 mA/cm^2. The phenol and COD abatement values, as well as the initial and final measured potentials, are shown in detail in Table S2 (SI) in Supplementary material. It was not possible to carry out the tests for Ti and TiO_2-NTs under the El-Ox current density of 0.75 mA/cm^2, as the two substrates reached the limit potential of the instrument (10 V) after just a few minutes.

In this case, the as-prepared electrodes containing non-crystalline manganese oxides reported similar phenol conversion efficiencies, probably because of the higher thickness of the MnO_x on the top of the NTs substrate, whose activity prevailed over that of the material within the pores. Nonetheless, the role of NTs played in reducing the final reaction potential was again confirmed.

The highest conversion was obtained for the *-2.5c_MnO$_x$/Ti* electrode, while the lowest one was reached for *2.5c_MnO$_x$/TiO$_2$-NTs*. Interestingly, as revealed by XRD, the higher the presence of α-MnO_2, the higher the conversion, while the higher the presence of α-Mn_2O_3, the lower is the degradation efficiency. The lower effectiveness of the latter type of electrodes could be due to the higher production of molecular oxygen, as Mn_2O_3 (Mn^{3+}) is considered the most active phase for water splitting [40,50,65,66], and it leads to the indirect oxidation of phenol through a reaction with O_2. MnO_2 (Mn^{4+}) is instead more active for phenol oxidation [24,25] or in heterogeneous catalysis [69,70], due to its ability to degrade organic molecules by producing hydroxil radicals (OH•). This has also been confirmed from the XPS analysis, which showed they were the samples with the highest AOS values (*i.e.* closer to the oxidation state

of Mn^{4+}). In addition, as for most of the samples, some intermediates of phenol decomposition were found in the solution treated with the *-2.5c_MnO$_x$/Ti* electrode, through an HPLC analysis (Fig. S12 in the SI), such as benzoquinone and hydroquinone, both of which are aromatic compounds. As reported in Fig. S12, maleic and fumaric acids, which are usually the first types of dicarboxylic acids obtained after ring opening, together with tartaric and oxalic acids, were determined as the most recurrent compounds. However, in some cases, malic, malonic, succinic, formic and acetic acids were also found in the treated solution. These by-products have also been identified in other works [71,72], thus confirming that the oxidation pathway for phenol is similar also for MnO_x electrodes: in the first step, phenol is oxidized to benzoquinone, which is in redox equilibrium with hydroquinone. The aromatic ring is opened and maleic and fumaric acids, which are *cis*-trans isomers, are formed. The oxidation then proceeds towards lower-weight acids, such as oxalic acid and, eventually, to mineralization.

Although the presence of nanotubes in the calcined material, induced a small reduction in the activity (~5%), the final potential was about 1 V lower in the *2.5c_MnO$_x$/TiO$_2$-NTs* sample than for the *2.5c_MnO$_x$/Ti* sample. This can be explained by considering the induced formation of both the α-Mn_2O_3 and α-MnO_2 phases on the TiO_2-NTs substrate. The LSV of the *2.5c_MnO$_x$/TiO$_2$-NTs* sample resulted in the highest current densities in 0.1 M Na_2SO_4 (Fig. 7), which showed a higher tendency of this electrode towards the water splitting reaction. This feature, *i.e.* greater stability and oxygen evolution activity, is worth exploiting using this type of electrode in mild Catalytic Wet Air Oxidation (CWAO) conditions (Temperature, T < 200 °C; Pressure, P < 30 bar), in order to be able to exploit the O_2 produced to degrade phenol in a high T – high P electrochemical multifunctional reactor.

The Faradaic efficiency (FE) was calculated from the COD conversion, using Eq. (3):

$$FE = \frac{COD - COD_0}{8I\Delta t} \cdot FV_r \quad (2)$$

where COD_0 and COD are the chemical oxygen demand before and after the test, F is Faraday's constant (96487C/mol), V is the reaction volume (l), I is the applied current (A) and Δt is the reaction time (s).

The Faradaic efficiency of the electrodes synthesized at 0.25 mA/cm^2 was higher for the samples grown on the nanotubes (see Table 2), because of the good performances obtained in terms of COD conversion.

The Faradaic efficiency was generally higher for the electrodes deposited at 2.5 mA/cm^2 (see Table 3), than for the ones observed for the samples synthesized at lower current densities, due to the fact that the conversion of both phenol and COD was much improved. In this case, with the exception of the *2.5c_MnO$_x$/TiO$_2$-NTs* electrode, the FE was similar for all the electrodes, even for those sample that showed a lower phenol conversion. This implies that phenol can be readily converted into more oxidized molecules, such as benzoquinone or maleic acid (see Fig. S12)), but any further degradation is more difficult, thus a difference between the phenol and COD conversions have been observed.

Even though the complete removal of phenol was not achieved, the specific activities of the MnO_x-based electrodes were quite high, as shown in Tables 2 and 3. The theoretical amount of Mn that was deposited on the electrode surfaces during the electrodeposition experiments can be calculated according to Faraday's law as:

$$I \cdot \Delta t = z \cdot \frac{m}{MW_i} \cdot F \quad (3)$$

where I is the electrodeposition current (A), Δt is the electrodeposition time, z is the number of electrons involved (2 for anodic deposition, 3 for cathodic deposition), m is the mass deposited (g), MW_i is the molecular weight of the ionic species (g/mol) and F is Faraday's constant (96487C/mol). Hence, the theoreticall amount of Mn in the electrodes deposited at 0.25, 2.5 or −2.5 mA/cm^2 for 10 min were 0.043, 0.427 and 0.285 mg_{Mn}/cm^2, respectively.

The Turn Over Number (TON) referred to the Mn (active sites) was then calculated as mols of phenol degraded by mols of Mn in the electrodes (see Tables 2 and 3). In the same manner, a conversion efficiency related to the energy consumption was calculated by dividing the TON by the total applied energy (in Wh) provided to the electrode during the 5 h of the degradation test and the results are also reported in the last column of Tables 2 and 3.

The TON for the electrodes deposited at 0.25 mA/cm^2 was lower for the samples grown on Ti than the one obtained for the films synthesized over the nanotubes, especially for the non calcined samples. The energy relative conversion followed the same trend, with the best performances being observed for samples on the TiO_2-NTs.

The electrodes deposited at 2.5 mA/cm^2, in general, led to lower TONs than the electrodes synthesized at 0.25 mA/cm^2, probably due to the elevated thickness of the films, which did not allow all the deposited manganese oxide to be exploited. As for the phenol degradation, the anodically deposited and calcined films and the samples grown on nanotubes were slightly less performing than the samples over titanium. However, the energy related conversion, had an inverse trend, with better results for the abovementioned electrodes. This was due to the improved stability and, thus, to the lower potential reached during the electrooxidation process.

The cathodic manganese oxides proved to be the best performing synthesized electrodes, for all the analyzed parameters (phenol degradation, COD reduction, TON and energy relative conversion).

A comparison was made with one of the most effective SnO_2-Sb sample on the TiO_2-NTs electrode [33], that converted 90% of phenol in 1.7 h, at a a current density of 10 mA/cm^2, which corrensponds to a working potential of about 2.85 V vs RHE. For this type of electrode the deposited mass was 2.50 mg/cm^2 and the TON was 0.88 mol_{Phenol}/mol_{SnSb}, which is similar to the one obtained for *-2.5c_MnO$_x$* and lower than the electrodes grown at 0.25 mA/cm^2 on the TiO_2-NTs. When the energy given to the electrode for 1.7 h was considered, the conversion related to the energy consumption was of 18.2 $mol_{Phenol}/(mol_{SnSb}\cdot Wh)$, that is, 58% less than our best electrode (*-2.5c_MnO$_x$/Ti*) which achieved 43.7 $mol_{Phenol}/(mol_{SnSb}\cdot Wh)$.

3.6 Accelerated lifetime tests

It was not possible to perform durability tests on the non-calcined electrodes, deposited at 0.25 mA/cm^2 or at 2.5 mA/cm^2, as those electrodes immediately reached 10 V. As a consequence, it is possible to state that calcination was essential to reach a resistant film that could withstand high current densities, without being damaged or reaching too high working potentials.

Fig. 12 shows the tests that were carried out on the calcined electrodes electrodeposited at 0.25 mA/cm^2 and it can be observed that films grown on TiO_2-NTs were able to resist up to 3 h, while the samples on Ti had a lifetime of about 2 h, with a slight increase in durability when the calcination occurred at a fast ramp (Fig. 12d).

Fig. 13 reports the results of the durability tests on the calcined electrodes electrodeposited at 2.5 mA/cm^2, among which the *2.5c_MnO$_x$/TiO$_2$-NTs* sample reached about 15 h of accelerated lifetime, while the same film deposited on metallic titanium stopped at 12 h. Both the *-2.5c_MnO$_x$/Ti* and *-2.5c_MnO$_x$/TiO$_2$-NTs* cathodic electrodes resisted for about 7 h, thus confirming that the calcined anodic samples were the most durable electrodes. If compared to previous literature works, the results obtained on the most stable sample were comparable in order of magnitude to the durability tests carried out for similar electrodes based on SnO_2-Sb synthe-

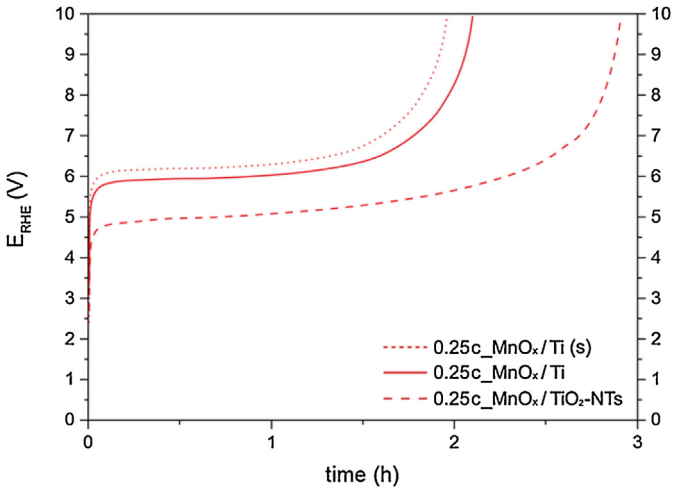

Fig. 12. Accelerated lifetime test at 100 mA/cm^2 in 1 M Na_2SO_4 of samples synthesized at 0.25 mA/cm^2.

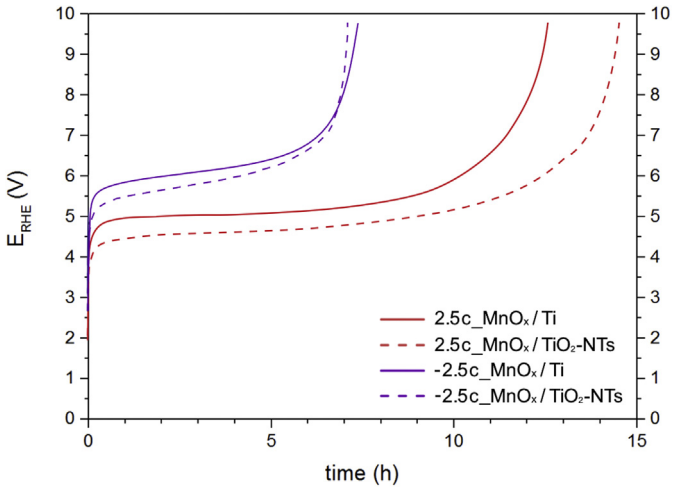

Fig. 13. Accelerated lifetime test at 100 mA/cm^2 in 1 M Na_2SO_4 of samples synthesized at 2.5 mA/cm^2.

sized *via* electrodeposition over TiO_2-NTs, which had durabilities of about 36 h [35].

4. Conclusions

In conclusion, MnO_x electrodeposited on titanium and titania nanotubes were synthesized, fully characterized and tested. Various techniques, which led to different morphologies and phases of manganese oxides, were employed, as reported by means of the FESEM, XRD and XPS investigations. In particular, α-MnO_2 on titanium demonstrated the highest activity for the electro-degradation of phenol, while α-Mn_2O_3 on titania nanotubes provided the highest stability during the reaction.

Synthesis on TiO_2-NTs allowed the manganese oxide to penetrate inside the nanotube array when anodic deposition was carried out, while cathodic deposition did not show any relevant growth of manganese oxide inside the nanotube structure. MnO_x deposited on TiO_2-NTs resulted in lower working potentials (about 1-1.5 V) during the electro-oxidation of phenol, than the same electrodes grown on Ti metal. This result was investigated through an EIS analysis, which confirmed the fundamental role of TiO_2-NTs in enhancing the charge transfer properties and improving the conduction from the metal substrate to the MnO_x film, especially in calcined electrodes, as the formation of a passivating layer of rutile on the metallic Ti was avoided. Thus, excellent performances were obtained on the optimized substrates, even though total phenol and COD conversions were not reached in this work. However, it is important to underline that the electro-oxidations were carried out at very low current densities with respect to those adopted in most of the literature. Furthermore, these results should be considered in relation to the amount of deposited material, which was lower than for the other reported syntheses, due to the fast electrodeposition times.

Moreover, the durability tests proved that the electrodes anodically deposited at high current densities had the longest lifetime, which was further increased by the presence of the nanotubes layer (up to 15 h), thanks to the better adhesion obtained from the penetration of the MnO_x film inside the nanotubes. More studies are required in order to better understand the deactivation causes, in order to be able to further improve the lifetime of these materials.

The easiness of the procedure and the thermal energy saving obtained with the proposed synthesis method should be considered as positive points, since there is no need for long layer by layer preparations, such as the one used to deposit alternate layers of Sb and Sn from their respective precursors solutions and for which the calcination times are higher. Hence, further improvements should be made to increase both the performance and stability of such electrodes, in order to find an interesting alternative to the commonly used, and more expensive (*e.g.* IrO_2, RuO_2) or more toxic electrodes (*e.g.* PbO_2) for the treatment of organics in wastewater. Moreover, the here presented results open interesting perspectives for additional phenol degradation studies, even under intensified process conditions. In fact, studies on electrodes contaning α-Mn_2O_3 (*e.g. 2.5c_MnOx/Ti* and *2.5c_MnOx/TiO2-NTs*), which is active for the water oxidation, are currently in progress in our laboratories, in order to exploit in-situ O_2 evolution, with the aim of boosting phenol conversion at high temperatures and high pressures and of analyzing the feasibility of process intensification of this technology.

Acknowledgments

This work has been funded by the EU Framework Program Horizon 2020: Project TERRA, Grant agreement number 677471 and Project CELBICON, Grant agreement number 679050). The authors would like also to thank Mauro Raimondo for conducting the FESEM analysis and Micaela Castellino for the XPS analysis.

Appendix A. Supplementary data

Supplementary data associated with this article can be found, in the online version, at http://dx.doi.org/10.1016/j.apcatb.2016.10.025.

References

[1] H.M. Pinheiro, E. Touraud, O. Thomas, Dyes Pigm. 61 (2004) 121–139.
[2] A.L. Buikema, M.J. McGinniss, J. Cairns, Mar. Environ. Res. 2 (1979) 87–181.
[3] R. Maciel, G.L. Sant'Anna Jr., M. Dezotti, Chemosphere 57 (2004) 711–719.
[4] K. Turhan, S. Uzman, Desalination 229 (2008) 257–263.
[5] F. Stüber, J. Font, A. Eftaxias, M. Paradowska, M.E. Suarez, A. Fortuny, C. Bengoa, A. Fabregat, Process Saf. Environ. Prot. 83 (2005) 371–380.
[6] F. Martínez, J.A. Melero, J.Á. Botas, M.I. Pariente, R. Molina, Ind. Eng. Chem. Res. 46 (2007) 4396–4405.
[7] G. Busca, S. Berardinelli, C. Resini, L. Arrighi, J. Hazard. Mater. 160 (2008) 265–288.
[8] C.Q.-Y. Wang Yun-Hai, Li Guo and Li Xiang-Lin, in: P.K.-Y. Show (Ed.), Industrial Waste, InTech. (2012), pp. 33-52.
[9] Á. Anglada, A. Urtiaga, I. Ortiz, J. Chem. Technol. Biotechnol. 84 (2009) 1747–1755.
[10] C. Comninellis, C. Pulgarin, J. Appl. Electrochem. 21 (1991) 703–708.
[11] D. Fino, C.C. Jara, G. Saracco, V. Specchia, P. Spinelli, J. Appl. Electrochem. 35 (2005) 405–411.

[12] M. Li, C. Feng, W. Hu, Z. Zhang, N. Sugiura, J. Hazard. Mater. 162 (2009) 455–462.
[13] C.C. Jara, D. Fino, G. Saracco, V. Specchia, Chem. Eng. Sci. 62 (2007) 5644–5647.
[14] J.C.d. Santos, J.C. Afonso, A.J.B. Dutra, J. Braz. Chem. Soc. 22 (2011) 875–883.
[15] S. Di Giulio, C. Carlesi Jara, D. Fino, G. Saracco, V. Specchia, P. Spinelli, Ind. Eng. Chem. Res. 46 (2007) 6783–6787.
[16] A.M. Polcaro, S. Palmas, F. Renoldi, M. Mascia, J. Appl. Electrochem. 29 (1999) 147–151.
[17] X. Chen, F. Gao, G. Chen, J. Appl. Electrochem. 35 (2005) 185–191.
[18] J.D. Rodgers, W. Jedral, N.J. Bunce, Environ. Sci. Technol. 33 (1999) 1453–1457.
[19] R.A. de Souza, L.M. Ruotolo, Int. J. Electrochem. Sci. 8 (2013) 643–657.
[20] M. Cataldo Hernández, N. Russo, M. Panizza, P. Spinelli, D. Fino, Diamond Relat. Mater. 44 (2014) 109–116.
[21] Y.-q. Wang, B. Gu, W.-l. Xu, J. Hazard. Mater. 162 (2009) 1159–1164.
[22] G. Sotgiu, M. Foderà, F. Marra, E. Petrucci, Chem. Eng. Trans. 41 (2014) 115–120.
[23] G. Sotgiu, L. Tortora, E. Petrucci, J. Appl. Electrochem. 45 (2015) 787–797.
[24] G.V. Sokol'skii, S.V. Ivanova, N.D. Ivanova, E.I. Boldyrev, T.F. Lobunets, T.V. Tomila, J. Water Chem. Technol. 34 (2012) 227–233.
[25] W.-c. Peng, S.-b. Wang, X.-y. Li, Sep. Purif. Technol. 163 (2016) 15–22.
[26] M. Nakayama, M. Shamoto, A. Kamimura, Chem. Mater. 22 (2010) 5887–5894.
[27] S.-W. Lee, C.-W. Lee, S.-B. Yoon, M.-S. Kim, J.H. Jeong, K.-W. Nam, K.C. Roh, K.-B. Kim, J. Power Sources 312 (2016) 207–215.
[28] M. Sawangphruk, P. Srimuk, P. Chiochan, A. Krittayavathananon, S. Luanwuthi, Carbon 60 (2013) 109–116.
[29] J. Jiang, A. Kucernak, Electrochim. Acta 47 (2002) 2381–2386.
[30] C. Ottone, M. Armandi, S. Hernández, S. Bensaid, M. Fontana, C.F. Pirri, G. Saracco, E. Garrone, B. Bonelli, Chem. Eng. J. 278 (2015) 36–45.
[31] F. Zhou, A. Izgorodin, R.K. Hocking, L. Spiccia, D.R. MacFarlane, Adv. Energy Mater. 2 (2012) 1013–1021.
[32] Y. Chen, L. Hong, H. Xue, W. Han, L. Wang, X. Sun, J. Li, J. Electroanal. Chem. 648 (2010) 119–127.
[33] Q. Wang, T. Jin, Z. Hu, L. Zhou, M. Zhou, Sep. Purif. Technol. 102 (2013) 180–186.
[34] Y. Chen, H. Li, W. Liu, Y. Tu, Y. Zhang, W. Han, L. Wang, Chemosphere 113 (2014) 48–55.
[35] G. Zhao, X. Cui, M. Liu, P. Li, Y. Zhang, T. Cao, H. Li, Y. Lei, L. Liu, D. Li, Environ. Sci. Technol. 43 (2009) 1480–1486.
[36] X. Cui, G. Zhao, Y. Lei, H. Li, P. Li, M. Liu, Mater. Chem. Phys. 113 (2009) 314–321.
[37] A. Lamberti, A. Sacco, S. Bianco, M. Quaglio, D. Manfredi, C.F. Pirri, Microelectron. Eng. 111 (2013) 137–142.
[38] D. Pugliese, A. Lamberti, F. Bella, A. Sacco, S. Bianco, E. Tresso, Org. Electron. 15 (2014) 3715–3722.
[39] S. Hernández, D. Hidalgo, A. Sacco, A. Chiodoni, A. Lamberti, V. Cauda, E. Tresso, G. Saracco, PCCP 17 (2015) 7775–7786.
[40] S. Hernández, C. Ottone, S. Varetti, M. Fontana, D. Pugliese, G. Saracco, B. Bonelli, M. Armandi, Materials 9 (2016) 296.
[41] G.F. Ortiz, I. Hanzu, T. Djenizian, P. Lavela, J.L. Tirado, P. Knauth, Chem. Mater. 21 (2009) 63–67.
[42] A. Lamberti, N. Garino, A. Sacco, S. Bianco, A. Chiodoni, C. Gerbaldi, Electrochim. Acta 151 (2015) 222–229.
[43] X. Lu, G. Wang, T. Zhai, M. Yu, J. Gan, Y. Tong, Y. Li, Nano Lett. 12 (2012) 1690–1696.
[44] S. Yoriya, H.E. Prakasam, O.K. Varghese, K. Shankar, M. Paulose, G.K. Mor, T.J. Latempa, C.A. Grimes, Sens. Lett. 4 (2006) 334–339.
[45] A. Lamberti, A. Virga, A. Chiado, A. Chiodoni, K. Bejtka, P. Rivolo, F. Giorgis, J. Mater. Chem. C 3 (2015) 6868–6875.
[46] P. Roy, S. Berger, P. Schmuki, Angew. Chem. Int. Ed. 50 (2011) 2904–2939.
[47] A. Lamberti, A. Chiodoni, N. Shahzad, S. Bianco, M. Quaglio, C.F. Pirri, Sci. Rep. 5 (2015).
[48] C. Wei, W. Ning, L. Li, C. Yanran, C. Xia, C. Quanjing, G. Lin, Nanotechnology 20 (2009) 445601.
[49] A. Ramírez, D. Friedrich, M. Kunst, S. Fiechter, Chem. Phys. Lett. 568–569 (2013) 157–160.
[50] A. Ramírez, P. Hillebrand, D. Stellmach, M.M. May, P. Bogdanoff, S. Fiechter, J. Phys. Chem. C 118 (2014) 14073–14081.
[51] E. Gemelli, N.H.A. Camargo, Matéria (Rio de Janeiro) 12 (2007) 525–531.
[52] M.N. Muti, A. Dzilal, J. Dennis, J. Eng. Sci. Technol. 3 (2008) 163–171.
[53] Z. Lockman, C.H. Kit, S. Sreekantan, J. Nucl. Relat. Technol. 6 (2009) 57–64.
[54] C.A. Grimes, G.K. Mor, TiO2 Nanotube Arrays: Synthesis, Properties, and Applications, Springer, US, Boston, MA, 2009, pp. 67–113.
[55] D. Siva Rama Krishna, Y. Sun, Surf. Coat. Technol. 198 (2005) 447–453.
[56] J. Niu, X. Liu, K. Xia, L. Xu, Y. Xu, X. Fang, W. Lu, Int. J. Electrochem. Sci 10 (2015) 7331–7340.
[57] M. Sun, B. Lan, T. Lin, G. Cheng, F. Ye, L. Yu, X. Cheng, X. Zheng, Cryst. Eng. Comm. 15 (2013) 7010–7018.
[58] M.V. Tran, A.T. Ha, P.M.L. Le, J. Nanomater (2015) (2015).
[59] S.C. Pang, M.A. Anderson, T.W. Chapman, J. Electrochem. Soc. 147 (2000) 444–450.
[60] A. Taguchi, S. Inoue, S. Akamaru, M. Hara, K. Watanabe, T. Abe, J. Alloys Compd. 414 (2006) 137–141.
[61] G.A.M. Ali, M.M. Yusoff, Y.H. Ng, H.N. Lim, K.F. Chong, Curr. Appl. Phys. 15 (2015) 1143–1147.
[62] T. Nguyen, M. João Carmezim, M. Boudard, M. Fátima Montemor, Int. J. Hydrogen Energy 40 (2015) 16355–16364.
[63] A. Biswal, B. Tripathy, T. Subbaiah, D. Meyrick, M. Ionescu, M. Minakshi, Metall. Mater. Trans. E 1 (2014) 226–238.
[64] P.M.L. Le, T.A.N. Nguyen, M. Van Tran, Electrodeposited manganese oxide for electrochemical capacitor: effect of substrates on the capacitive behavior of electrodes, meeting abstracts, Electrochem. Soc. (2014) (177-177).
[65] T. Takashima, K. Hashimoto, R. Nakamura, J. Am. Chem. Soc. 134 (2012) 18153–18156.
[66] T. Takashima, K. Hashimoto, R. Nakamura, J. Am. Chem. Soc. 134 (2012) 1519–1527.
[67] S. Hernández, M. Tortello, A. Sacco, M. Quaglio, T. Meyer, S. Bianco, G. Saracco, C.F. Pirri, E. Tresso, Electrochim. Acta 131 (2014) 184–194.
[68] Y.-G. Huang, X.-H. Zhang, X.-B. Chen, H.-Q. Wang, J.-R. Chen, X.-X. Zhong, Q.-Y. Li, Int. J. Hydrogen Energy 40 (2015) 14331–14337.
[69] E. Saputra, S. Muhammad, H. Sun, H.M. Ang, M.O. Tadé, S. Wang, Environ. Sci. Technol. 47 (2013) 5882–5887.
[70] H. Zhao, Y. Dong, P. Jiang, G. Wang, J. Zhang, K. Li, C. Feng, New J. Chem. 38 (2014) 1743–1750.
[71] N.D. Mu'azu, M.H. Al-Malack, J. Environ. Tech. 5 (2012) 460.
[72] X.-y. Li, Y.-h. Cui, Y.-j. Feng, Z.-m. Xie, J.-D. Gu, Water Res. 39 (2005) 1972–1981.